Sediment storage by vegetation in steep bedrock landscapes: Theory, experiments, and implications for postfire sediment yield

Michael P. Lamb,[1] Mariya Levina,[1] Roman A. DiBiase,[1] and Brian M. Fuller[1]

[1]   Mechanistic models for sediment transport on hillslopes are needed for applications ranging from landscape evolution to debris-flow hazards. Progress has been made for soil-mantled landscapes; however, little is known about sediment production and transport in bedrock landscapes that often maintain a patchy soil mantle, even though slopes exceed the angle of repose. Herein we investigate the hypothesis that patchy soil cover is stable on steep slopes due to local roughness such as vegetation dams that trap sediment upslope. To quantify local sediment storage, we developed a new theory and tested it against tilt-table experiments. Results show that trapped sediment volume scales with the cube of dam width. Where the dam width is less than about fifty grain diameters, particle force chains appear to enhance stability, resulting in greater trapped volumes and sediment-pile slopes that exceed the angle of repose. Trapped volumes are greatest for hillslopes that just exceed the friction slope and are independent of hillslope gradient for gradients greater than about twice the friction slope. For neighboring dams spaced less than about five grain diameters apart, grain bridging results in a single sediment pile that is larger than the sum of individual piles. This work provides a mass-conserving framework for quantifying sediment storage and nonlocal transport in bedrock landscapes. Results may explain the rapid increase in sediment yield following wildfire in steep terrain in the absence of rainfall; as sediment dams are incinerated, particles become gravitationally unstable and move rapidly downslope as dry ravel.

1.   Introduction

[2]   Sediment storage and transport on hillslopes are important processes in landscape evolution, hazard mitigation associated with mass failures and debris flows, and hillslope-channel connectivity [e.g., *Burbank et al.*, 1996; *Lave and Burbank*, 2004; *Korup*, 2006; *Korup and Schlunegger*, 2007; *Perron et al.*, 2009; *Cannon et al.*, 2010]. For example, bedrock incision rates in channels may be strongly controlled by both the flux and the particle size of sediment delivered from neighboring hillslopes [e.g., *Sklar and Dietrich*, 2004; *Lamb et al.*, 2008]. Major advances have been made in understanding soil production and hillslope sediment-transport rates in landscapes with thick ($>\sim 0.1$ m) soil mantles [e.g., *Heimsath et al.*, 1997; *Roering et al.*, 1999]. The same is not true, however, in landscapes with thin ($<\sim 0.1$ m) or patchy soil mantles and partial exposure of bedrock (herein referred to as bedrock landscapes), although notable progress is being made [*Clarke and Burbank*, 2010; *DiBiase et al.*, 2012; *Heimsath et al.*,

2012]. Sediment transport in bedrock landscapes represents a major gap in our knowledge since many tectonically active orogens are dominated by steep bedrock terrain where gravitational instability and nonlocal transport may dominate over more diffusive soil-transport processes [e.g., *Burbank et al.*, 1996; *Clarke and Burbank*, 2010; *Foufoula-Georgiou et al.*, 2010].

[3]   Commonly applied models for hillslope sediment flux show that sediment flux tends to infinity at slopes that exceed a threshold for soil stability [*Roering et al.*, 1999; *Gabet*, 2003]. This approximation captures the effects of landsliding, rockfall, and dry ravel [e.g., *Roering et al.*, 2001]. Thus, according to such models, steep slopes should be devoid of sediment cover because any sediment produced from bedrock should be rapidly transported downslope. This notwithstanding, bare bedrock slopes entirely devoid of sediment cover are rare in mountain terrain [e.g., *DiBiase et al.*, 2010; *DiBiase et al.*, 2012; *Heimsath et al.*, 2012]. Instead, steep hillslopes commonly show a patchy soil mantle implying local stability (Figure 1). Sediment transport in these landscapes must be limited by sediment supply, and given strong feedbacks that exist between soil thickness, soil production rates, and landscape evolution [e.g., *Anderson*, 2002; *Tucker and Hancock*, 2010], it is important to quantify local sediment storage as a control on sediment production and transport.

[4]   Steep bedrock landscapes often produce large and sudden fluxes of sediment following wildfire that can fuel

[1]Geological and Planetary Sciences, California Institute of Technology, Pasadena, California, USA.

Corresponding author: M. P. Lamb, Geological and Planetary Sciences, California Institute of Technology, Pasadena, CA 91125, USA. (mpl@gps.caltech.edu)
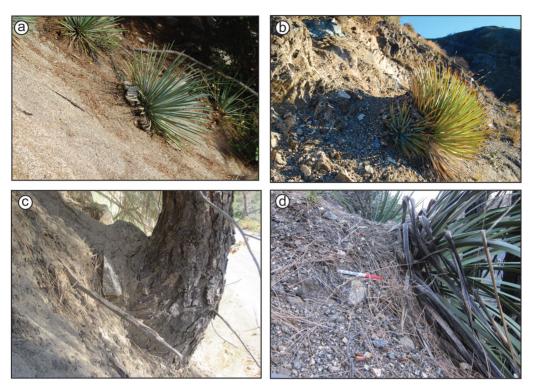
Figure 1. Sediment trapped behind (a, b, d) yucca plants in the San Gabriel Mountains, CA, and (c) pine trees in the Sierra Nevada Mountains, CA. The basal plant widths are approximately 0.6 m in Figure 1a, 0.3 m in Figure 1b, 0.5 m in Figure 1c, and 0.5 m in Figure 1d (14 cm pen for scale).

debris flows and sediment-laden floods resulting in loss of life and property [*Eaton*, 1935; *Rice*, 1982; *Wells*, 1987; *Gartner et al.*, 2008; *Cannon et al.*, 2010; *Kean et al.*, 2011]. Fire-induced sediment yield can exceed background rates by more than an order of magnitude in steep mountain terrain [*Wells*, 1981; *Rice*, 1982; *Moody and Martin*, 2001; *Lave and Burbank*, 2004; *Jackson and Roering*, 2009; *Lamb et al.*, 2011]. Numerical and conceptual models developed for soil-mantled landscapes suggest that fire-induced sediment flux leads to a heightened rate of soil production, and therefore, fire affects the long-term hillslope erosion rate over time scales relevant for landscape evolution [*Swanson*, 1981; *Gabet and Dunne*, 2003; *Lave and Burbank*, 2004; *Roering and Gerber*, 2005]. However, in steep bedrock landscapes, sediment transport is likely supply limited, consistent with observations of large patches of bedrock freshly exposed following wildfire [*Jackson and Roering*, 2009; *Schmidt et al.*, 2011]. In steep landscapes, enhanced sediment yield following fire may result from transient sediment storage by vegetation and release via dry ravel [e.g., *Rice*, 1982; *Gabet*, 2003; *Lave and Burbank*, 2004; *Jackson and Roering*, 2009; *Gabet and Mendoza*, 2012], which may not affect long-term soil production rates or landscape evolution [*Lamb et al.*, 2011]. For example, sediment commonly accumulates upslope of vegetation dams (Figure 1) [*Florsheim et al.*, 1991; *Fu*, 2004; *Shakesby and Doerr*, 2006]. When vegetation dams incinerate during wildfire, sediment released as dry ravel can be gravitationally unstable on steep slopes [*Florsheim et al.*, 1991; *Shakesby and Doerr*, 2006]. *Bennett* [1982] showed that the majority of postfire dry ravel yield occurs within 24 h of a wildfire and that ravel yields are significantly greater on slopes that exceeded the angle of

repose (~30°), which is common in other studies as well [*Anderson et al.*, 1959; *Krammes*, 1965; *Gabet*, 2003; *Jackson and Roering*, 2009]. Despite these important observations, most workers necessarily rely on empirical multiregression analyses to predict postfire sediment yield at a catchment scale [*Los Angeles County Flood Control District (LACFCD)*, 1959; *Gartner et al.*, 2008; *Cannon et al.*, 2010] in part because we lack mechanistic, mass-conserving transport models for bedrock landscapes.

[5] Herein we propose that patchy sediment cover in steep bedrock terrain results in part from vegetation (including plant stems, basal branches, and litter) and bedrock roughness that cause local reductions in slope allowing sediment stability. To build a mechanistic model for transient sediment storage and release by local roughness, we need to quantify the sediment-trapping capacity of vegetation [*Lamb et al.*, 2011]. *Fu* [2004] attempted to address this issue by assuming that trapped sediment builds a pyramidal wedge with side and top angles equal to the angle of repose, assumptions that have not been verified in the laboratory or the field. *DiBiase and Lamb* [2013] measured pile dimensions in the field but did not systematically explore different slopes or particle sizes. Thus, fundamental questions remain unanswered on the controls on sediment storage and potential postfire sediment yield in bedrock landscapes. How does the amount of trapped sediment depend on vegetation size and hillslope gradient? Is the amount of trapped sediment a function of sediment size? In regions with dense vegetation cover, do neighboring vegetation dams interact?

[6] To begin to answer these questions, we performed a series of laboratory experiments using a tilt table to measure the maximum volume of sediment that can be trapped

behind a dam. Experiments have been used previously to explore local and nonlocal sediment transport on hillslopes [*Roering et al.*, 2001; *Gabet and Mendoza*, 2012], but to our knowledge, no study has quantified sediment storage by dams on slopes that exceed the angle of repose. In this paper, we first develop a theory for the volume of sediment trapped behind a dam using dimensional analysis. Next we discuss the experimental setup and show results for a wide range of dam widths, sediment sizes, hillslope gradients, and spacings between multiple dams. Finally, we discuss the implications of our results for natural landscapes and postfire sediment yield.

2. Theoretical Framework

[7] Mass balance dictates that the maximum postfire sediment yield due to dry ravel can be calculated from the product of (1) the areal vegetation density for slopes that exceed the angle of repose and (2) the maximum mass of sediment trapped behind each plant [*Lamb et al.*, 2011]. Field and remotely sensed data can be used to calculate areal vegetation density; however, no theory or measurements exist for the maximum amount of trapped sediment by vegetation on steep slopes. Our goal here is fill this gap and develop a mechanistic, predictive geometric model for the maximum amount of sediment that can be trapped by an individual plant. We first attempt to understand the controls on sediment trapping behind a single dam, and in section 4.5, we consider the interaction of closely spaced dams as a first step to expanding these predictions to the catchment scale.

[8] Our theory is formulated for dams that are taller than approximately half their basal width, as is typical for plants, so that the maximum volume of sediment trapped is limited by the dam width rather than the dam height (Figure 2). Many of the concepts presented here should hold for short and wide dams, but the formulation would need to be adjusted to allow for pile-height limitations. In the absence of a pile-height limitation, we hypothesize that the volume of sediment trapped behind a dam (V) may depend on the width of the dam (W), characteristic particle diameter (D), hillslope gradient [S, here defined as the tangent of the hillslope angle (dimensionless)], the maximum slope of stability for individual grains on the bedrock surface [herein referred to
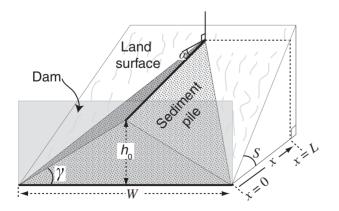
as the friction slope S_f, i.e., tangent of the friction angle (dimensionless)], and the maximum stable slope that a heap of grains maintains as a cone [S_r, i.e., tangent of the angle of repose (dimensionless)] (Figure 2). To synthesize the controlling variables, we use dimensional analysis, which indicates that the normalized volume of trapped sediment $\left(\frac{V}{(W+D)^3}\right)$ may be a function of four dimensionless variables, i.e.,

$$\frac{V}{(W+D)^3} = f\left(\frac{D}{W+D}, S, S_r, \frac{S-S_f}{S_f}\right) \tag{1}$$

where the terms $\frac{D}{W+D}$ and $\frac{S-S_f}{S_f}$ are referred to as the normalized sediment diameter and the normalized slope, respectively. Note that we choose $W+D$ as the normalization length scale rather than W because the sediment pile width may be larger than the dam width as particles can protrude by about $0.5D$ on either side of the dam.

[9] It is useful to approximate the geometry of sediment piles as oblique triangular pyramids [*Fu*, 2004] of height $h(x)$ and width $w(x)$, where x is the horizontal coordinate in the direction of the maximum slope, the dam is located at $x = 0$, and the upslope extent of the pile is at $x = L$ (Figure 2). Thus, the volume of the pile can be found from

$$V = \int_0^L \frac{1}{2} w(x)h(x)dx. \tag{2}$$

[10] The angle of the side of the pile γ with respect to horizontal and in the direction perpendicular to the hillslope gradient is

$$\tan\gamma = \frac{2h_0}{(W+D)} \tag{3}$$

where $h_0 = h(x=0)$ (Figure 2). Likewise, by geometry, the angle of the ridge at the top of the pile α with respect to horizontal in the x direction is

$$\tan\alpha = S - \frac{h_0}{L}. \tag{4}$$

[11] Thus, the pile height and width at a given location along the x coordinate, and total pile length can be written as

$$h(x) = h_0 + x(S - \tan\alpha) \tag{5}$$

$$w(x) = (W+D) - 2x\left(\frac{S - \tan\alpha}{\tan\gamma}\right) \tag{6}$$

$$L = \frac{1}{2}\frac{(W+D)\tan\gamma}{(S - \tan\alpha)}. \tag{7}$$

[12] Under the assumption of uniform sloping pile sides (i.e., $\tan\gamma \neq f(x)$) and a linear top ridge (i.e., $\tan\alpha \neq f(x)$), equations (2) and (5)–(7) can be combined and integrated to yield

$$\frac{V}{(W+D)^3} = \frac{1}{24}\frac{\tan^2\gamma}{S - \tan\alpha}. \tag{8}$$

[13] The normalized pile volume thus depends on hillslope gradient and the pile slopes (i.e., $\tan\gamma$ and $\tan\alpha$),

Figure 2. Schematic showing a pyramidal sediment pile with height (h_0), length (L), top angle (α), and side angle (γ) that is trapped behind a dam of width W.

which following equation (1) may be a function of $\frac{D}{W+D}, S, S_r$ or $\frac{S-S_f}{S_f}$. In the following sections of this paper, we show results from experiments designed to test for this dependence.

3. Experimental Setup and Methods

[14] The goal of the experiments is to quantify the maximum volume of sediment trapped behind a vegetation or rock dam. The benefit of pursuing these measurements in the laboratory rather than the field is the ability to systematically vary one of the dimensionless parameters in equation (1) while holding the other dimensionless variables constant. In addition, a number of simplifications to the natural system can be made in the laboratory that allow us to explore a finite and tractable set of variables. In particular, the dam in all experiments was a smooth, vertical, planar wall made of Plexiglas with a finite height that was greater than the dam width (W) (Figure 3). Dam widths ranged from 20 to 384 mm in different experiments. The dam was positioned at the base of the tilt table (Figure 3), and we explored a range of tilt-table surface materials with varying roughness: Plexiglas, 80 grit sandpaper (equivalent to a roughness length scale of 0.192 mm), and a layer of particles with $D = 2.8$ mm glued to the table surface.

[15] We used eight different size classes of natural, rounded to subangular, siliceous sand and gravel with near-uniform
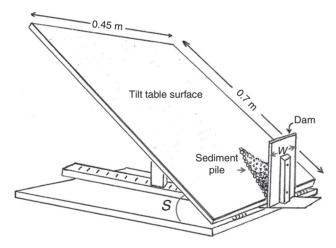

Figure 3. Schematic of the experimental tilt table that has an adjustable slope (S is tangent of the table angle), dam width (W), and table surface roughness.

size distributions (Table 1). We refer to each sediment-size class by the largest bounding value and use this value for subsequent calculations (i.e., D). The angle of repose of the seven sediment-size classes, measured using the dam-break method [*Vanburkalow*, 1945], range from 31° to 40° (i.e., $0.59 < S_r < 0.84$). To measure the friction slope, we randomly placed individual particles on the table and tilted it until the particles rolled off [e.g., *Buffington et al.*, 1992]. The angle of stability was noted for each particle, more than 100 measurements were made for a given particle-size class and table roughness, and the friction angles reported here are the mean values from these measurements. Friction angles were measured for all particle-size classes on the Plexiglas board, and results range from 23° to 26° ($0.43 < S_f < 0.48$). Friction angles also were measured for $D = 0.28$ mm for all three board surfaces, and results show a dramatic increase in S_f from 24.5° for Plexiglas to 39.5° for the 2.8 mm grain board (Table 1).

[16] During an experiment, the tilt table slope was set, and sediment was gently fed from upslope by hand to minimize the disturbance to the pile. Again, our goal was to measure maximum sediment storage; pile sizes in the field may be smaller if they are not at full capacity [*Lamb et al.*, 2011] or if capacity cannot be reached because grain inertia disturbs the pile. Once the pile reached its maximum size (Figure 4), the pile dimensions (h_0, L; Figure 2) and weight (using a scale accurate to 0.1 g) were recorded. Using these measurements, pile side angles and top angles were calculated using equations (3) and (4). Weight was converted to sediment volume using the bulk density of the sediment pile, $\rho_b \approx (1-p)\rho_s$, where p is the porosity and $\rho_s = 2650$ kg/m^3 is the sediment density. Porosity was measured by filling a graduated cylinder with sediment and weighing the amount of water added to submerge the grains, and these values range from 41.8% to 45% (Table 1). All sediment volume data presented herein were found from measurement of sediment mass (i.e., they are independent of the assumption of oblique triangular pyramids), and these data in turn are compared to the pyramidal model for sediment volume [i.e., equation (8)].

4. Controls on Sediment Storage: Results and Discussion

[17] In total, 255 experiments were performed with unique combinations of the dimensionless parameters in equation (1) (Table 2). In most cases, each experiment was repeated 5–8 times; however, some experiments were performed only

Table 1. Sediment and Friction Properties

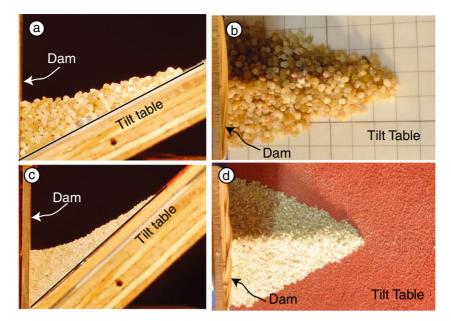| Grain Diameter (mm)	Angularity	Porosity (%)	Angle of Repose, S_r	Friction Angle, S_f		
				Plexiglas	0.192 mm Sandpaper	2.8 mm Grain Board
1	Subangular	45	0.64	0.48	–	–
1.0–2.0	Subangular	43	0.61	0.48	–	–
2.0–2.8	Rounded	41.8	0.62	0.45	0.55	0.88
2.8–4.0	Rounded	42.2	0.59	0.45	–	–
4.0–5.6	Mix of rounded and subangular	43.8	0.67	0.45	–	–
5.6–8.0	Subrounded to subangular	43.3	0.75	0.43	–	–
8.0–11.2	Subrounded to subangular	42.1	0.83	0.43	–	–
11.2–16.0	Subrounded	43.9	0.84	0.43	–	–

Figure 4. Photographs of the experimental ravel piles in side view and plan view from experiment set 3 with $S=0.52$, $W=56$ mm, $D=2.8$ mm and a smooth Plexiglas table in Figures 4a and 4b, and $S=0.92$, $W=56$ mm, $D=1.0$ mm and a 0.192 mm roughness sandpaper table in Figures 4c and 4d. The pile dimensions at the dam were height$=24$ mm in Figure 4a, width$=56$ mm and 10 mm grid spacing in Figure 4b, height$=25$ mm in Figure 4c, and width$=56$ mm in Figure 4d.

Table 2. Summary of Experiment Sets

Experiment Set	Slope, S	Grain Diameter, D (mm)	Dam Width, W (mm)	Gap Spacing, λ (mm)	Table Roughness	Number of Experiments	Normalized Slope $(S-S_f)/S_f$	Normalized Grain Diameter $D/(W+D)$	Normalized Gap Spacing λ/D
1	0.78	1.0–16.0	20–384	0	Plexiglas	57	1.64–1.82	0.0026–0.44	0
2	0.42–2.67	2.8–5.6	28–56	0	Plexiglas, sandpaper, grain board	92	1.0–6.01	0.091	0
3	0.46–1.80	2.8–5.6	56–112	0	Plexiglas, sandpaper, grain board	28	1.0–4.01	0.048	0
4	0.78	2.0–4.0	20–40	0–40	Plexiglas	78	1.64–1.75	0.091	0–14.23

The number of experiments refers to the number of experiments where at least one variable was different. Most experiments were repeated five to eight times to assess intrinsic variability and measurement error.

once. The mean or geometric mean of these repeat experiments is reported, and the standard deviation or the geometric standard deviation is shown as error bars that combine both the experimental error and the stochastic nature of grain piles. In this section, we first show results on the controls on pile volume that include dam width, normalized slope, and normalized grain size. Second, we formulate empirical models for the pile top and side angles as functions of normalized slope and grain size. Finally, these empirical relationships for pile angles are incorporated into a geometric model for pile volume [equation (8)], which in turn is compared to independent measurements of pile volume as a function of dam width, normalized sediment size, hillslope gradient, and multiple interacting dams.

4.1. Effect of Dam Width on Pile Volume

[18] As indicated by equations (1) and (8), the first-order control on the volume of trapped sediment was the width of the dam (Figure 5); when the other dimensionless variables were held constant, $V \propto (W+D)^3$. However, the data also show that pile size tended to be larger with larger normalized particle sizes $\left(\frac{D}{W+D}\right)$ for cases where S and S_f were held constant (Figure 5a). In addition, pile volume tended to be larger for larger friction slopes (i.e., smaller $\frac{S-S_f}{S_f}$) for cases where $\frac{D}{W+D}$ was held constant (Figure 5b). If the assumption of pyramidal pile geometry is correct [i.e., equation (8)], as verified in the next section, then the dependence of pile volume on normalized slope and normalized grain diameter indicates that the pile top angle (tan α) or the side angle (tan γ) or both are not constant, but functions of $\frac{D}{W+D}$ or $\frac{S-S_f}{S_f}$.

4.2. Pyramidal Geometry Assumption

[19] To verify the pyramidal geometry assumption, we calculated the pile angles (i.e., tan γ and tan α; Figure 2) from the measurements of pile height and length following equations (3) and (4). The calculated normalized pile
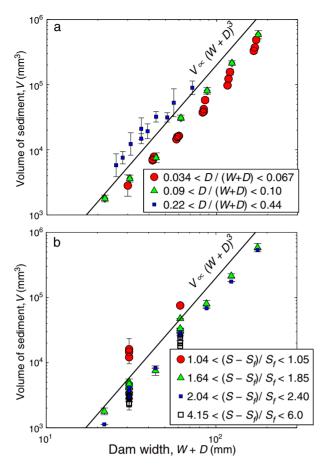
Figure 5. Measured volume of sediment piles as a function of dam width for (a) different normalized sediment diameters ($D/(W+D)$) and nearly constant normalized slope ($1.6 < (S - S_f)/S_f < 1.85$) and (b) different normalized slopes with constant normalized sediment diameter ($D/(W+D) = 0.091$). Solid lines in both plots show a cubic relationship. Data are from experiment sets 1–3. Symbols represent geometric means, and error bars represent one geometric standard deviation from five to eight repeat experiments. Symbols without error bars either are from a single experiment or have an error less than the symbol size.
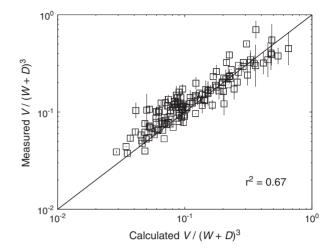

Figure 6. Measured normalized pile volume versus the normalized pile volume calculated from equation (8) and the measured pile top and side angles from experiment sets 1–3. The solid line shows a 1:1 correspondence and verifies the assumption of representing the pile as a pyramid. Symbols represent geometric means, and error bars represent one geometric standard deviation from five to eight repeat experiments. Symbols without error bars either are from a single experiment or have an error less than the symbol size.

volumes, assuming a pyramidal geometry, match well the actual measured normalized volumes for values spanning more than an order of magnitude (Figure 6). The scatter in the data is in part from the piles deviating from this geometry and from the experimental error. For example, visual inspection indicated that the piles often deviated from a pyramid just upslope of the dam (generally within $x < a_1 D$, where $a_1 \sim 10$), where the local top angle tended to be small (i.e., concave-up top surface; Figure 4). This notwithstanding, the pyramidal assumption was in general robust ($r^2 = 0.67$), it greatly simplifies building a model for pile geometry, and therefore, we adopt it for the rest of the analysis to evaluate the effects of $\frac{D}{W+D}$, S, S_r, and $\frac{S - S_f}{S_f}$ on pile geometry.

4.3. Effect of Normalized Particle Size on Pile Geometry

[20] Experiment set 1 was designed to explore the effect of normalized particle size $D/(W+D)$ on pile volume with all other dimensionless parameters held approximately constant (Table 2). For all experiments in this set, we used a smooth Plexiglas surface on the tilt table, and the table angle was held constant at $S = 0.78$. Although different particle-size classes were used (with variable angularity), the table friction angle was within a narrow range for all cases ($0.43 < S_f < 0.48$) (Table 1).

[21] Results show that the pile top angle ($\tan \alpha$), calculated from measurements of pile height and length [i.e., equation (4)], was relatively insensitive to sediment size, whereas the pile side angle ($\tan \gamma$), calculated from measurements of pile height and dam width [i.e., equation (3)], increased with increasing D, albeit with substantial data scatter (Figure 7a). As expected from our dimensionless framework, the data for $\tan \gamma$ appear to collapse to a single relationship when plotted against $D/(W+D)$ rather than D alone, with an increase in $\tan \gamma$ to values well above the angle of repose for $D/(W+D) > 0.1$ (Figure 7b). The increase in pile side angle with increasing normalized particle size cannot be explained by changes in the particle angularity or any other particle specific property. For example, Figure 7c shows that the trend of increasing $\tan \gamma$ with increasing $D/(W+D)$ occurred even within individual grain-size classes. Thus, the trend persisted regardless of whether D was varied in the experiments (with constant W), or whether W was varied in experiments that used the exact same sediment. In other words, the observed effect is fundamentally due to the change in the ratio of $D/(W+D)$. Why did this occur?

[22] Unlike a heap of particles on a horizontal surface, the particles on a tilt table are inherently unstable without the presence of the dam. Thus, there is a downslope force due to the weight of the particles on the dam and an equal and opposite force from the dam onto the particles. We hypothesize that this results in a net compressive stress in the x direction, which in turn produces enhanced frictional
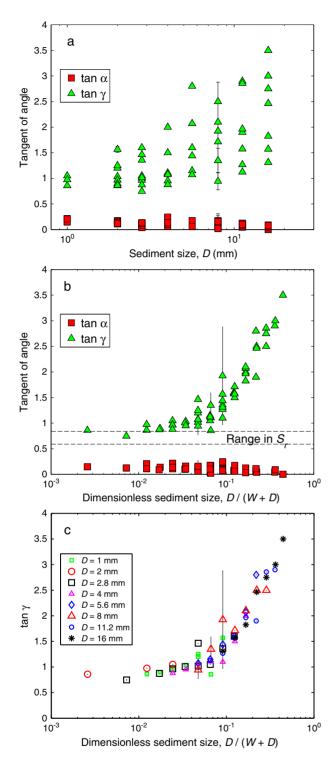
Figure 7. Pile top (tan α) and side (tan γ) angles as a function of (a) sediment diameter and (b) normalized sediment diameter, and (c) pile side angle as a function of normalized sediment diameter for discrete grain-size classes. Figure 7b shows the range in angles of repose (S_r) for the different sediment used in the experiments. Data are from experiment set 1. Symbols represent means, and error bars represent one standard deviation from five to eight repeat experiments. Symbols without error bars either are from a single experiment or have an error less than the symbol size.

stresses at particle-particle contacts, increasing pile side angles to values that exceed the angle of repose. The compressive stress at individual particle contacts is greater for larger values of $D/(W+D)$ because, with all other factors equal (including the downslope weight of the pile), there are fewer particle contacts with larger $D/(W+D)$ and, hence, a larger compressive stress accommodated per particle contact. In other words, the total number of particles in the pile (n_b) scales as $n_b \propto \frac{V}{V_p} \propto \frac{(W+D)^3}{D^3}$, where V_p is the particle volume. Moreover, previous workers have shown that forces are often distributed through granular media by discrete force chains with characteristic lengths (L_f) of $L_f \propto D$ with a proportionality constant of order 10 [*Cates et al.*, 1998; *Furbish et al.*, 2008; *Estep and Dufek*, 2012]. Thus, we expect the enhanced particle-particle friction due to downslope-oriented compressive stresses to become important when the characteristic pile length scale is less than the force-chain length scale (i.e., $(W+D) \leq L_f$ and $L_f \approx a_1 D$). To account for this effect, we propose

$$\frac{\tan \gamma}{S_r} - 1 = a_1 \left(\frac{D}{(W+D)} S \right)^{a_2} \quad (9)$$

where a_1 and a_2 are empirical constants. Thus, for $D/(W+D) \ll a_1$, or for very low slopes, force chains are negligible, and equation (9) predicts that the side angle is approximately the angle of repose. Alternatively, when $D/(W+D) > a_1$, $\tan \gamma > S_r$ due to the effect of force chains and compressive stresses induced by the dam. The data from experiment sets 1–3 appear to support the construct of equation (9) (Figure 8), and we find the best fit values to be $a_1 = 5.8$ and $a_2 = 0.65$ ($r^2 = 0.71$).

4.4. Effect of Slope and Friction Slope on Pile Geometry

[23] Experiment sets 2 and 3 were designed to evaluate the effect of S and S_f on pile geometry while holding all
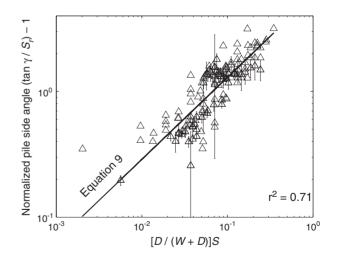

Figure 8. Power law fit of pile side angles as a function of the product of normalized sediment diameter and slope following equation (9). Data are from experiment sets 1–3. Error bars represent one geometric standard deviation from five to eight repeat experiments. Symbols represent geometric mean of tan γ. Symbols without error bars either are from a single experiment or have an error less than the symbol size.

other dimensionless variables approximately constant. Both experiment sets 2 and 3 used the same sediment ($D = 2.8$ mm, $S_r = 0.62$), a range of board slopes, and three different board roughness conditions, thereby producing three different values of S_f (0.45, 0.55, and 0.88). The only difference between the experiment sets is that experiment set 2 used a 28 mm wide dam (i.e., $D/(W+D) = 0.091$), whereas experiment set 3 had $W = 56$ mm (i.e., $D/(W+D) = 0.048$).

[24] We found that the pile side angle, $\tan \gamma$, was relatively insensitive to slope and friction slope for both experiment sets (Figure 9). The side angles were larger for experiment set 2 (Figure 9a) compared to experiment set 3 (Figure 9b), which is consistent with the about twofold decrease in $D/(W+D)$ as discussed in section 4.3. Data from both experiment sets also show a slight increase in $\tan \gamma$ with increasing

S, and data with different S_f collapse to nearly the same trend (Figure 9), consistent with equation (9).

[25] In contrast to the side angle, the pile top angle $\tan \alpha$ was sensitive to both S and S_f (Figure 9). In general, experiments with larger S_f produced larger top angles. The change in $\tan \alpha$ with S was more complicated, however, where $\tan \alpha$ decreased with increasing S for values of S just larger than S_f, and $\tan \alpha$ increased with S for values of S much larger than S_f. We are unsure what causes these trends. Through trial and error, we found that the data from experiment sets 2 and 3 both collapse to a single power law relationship, i.e.,

$$\tan \alpha - S = a_3 \left(\frac{S - S_f}{S_f} \right)^{a_4} \qquad (10)$$

where best fit values of the empirical constants are $a_3 = 0.9$ and $a_4 = 0.6$ (Figure 10) ($r^2 = 0.83$). This relationship appears to be robust regardless of variations in S_f (Figure 10a) or $D/(W+D)$ alone (Figure 10b), although data with $S_f = 0.88$ are shifted to slightly greater top angles. At the
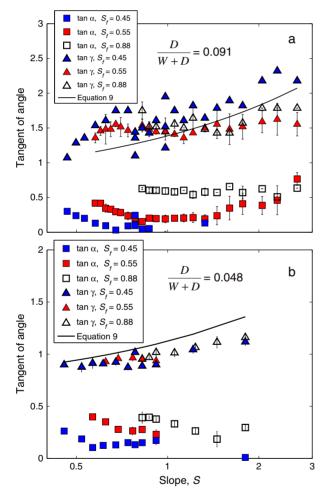

Figure 9. Pile side and top angles as functions of table slope for three different board roughness scales (Plexiglas, 0.192 mm sandpaper, and 2.8 mm grain board that correspond to the three friction slopes) with (a) $D/(W+D) = 0.091$ (experiment set 2) and (b) $D/(W+D) = 0.048$ (experiment set 3). The solid line in both panels corresponds to the model prediction for the pile side angle ($\tan \gamma$) given by equation (9) (Figure 8). Symbols represent means, and error bars represent one standard deviation from five to eight repeat experiments. Symbols without error bars either are from a single experiment or have an error less than the symbol size.
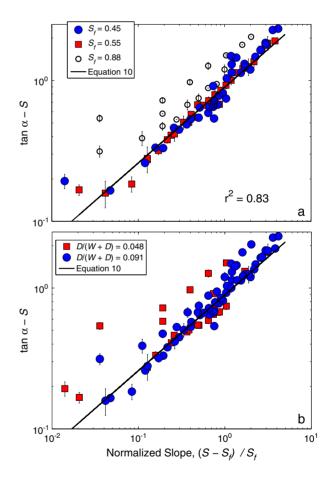

Figure 10. Pile top angle minus slope as a function of normalized slope following equation (10) showing that data collapse regardless of (a) the friction slope and (b) the normalized particle diameter. Data in both panels are the same and from experiment sets 2 and 3. Symbols represent geometric means, and error bars represent one geometric standard deviation from five to eight repeat experiments. Symbols without error bars either are from a single experiment or have an error less than the symbol size.

lower limit of $S = S_f$, equation (10) predicts $\tan\alpha = S$, which, given the pyramidal assumption [equation (8)], reproduces the expected finding of an infinite volume of trapped material for slopes less than or equal to the friction slope (i.e., a soil-mantled landscape).

4.5. Combined Model for Sediment Pile Volume

[26] Equations (8)–(10) can be combined to yield a semiempirical geometric model for pile volume, i.e.,

$$\frac{V}{(W+D)^3} = \frac{1}{24} \frac{S_r^2 \left[1 + a_1 \left(\frac{D}{(W+D)} S \right)^{a_2} \right]^2}{a_3 \left(\frac{S-S_f}{S_f} \right)^{a_4}}. \tag{11}$$

[27] Using all data from experiment sets 1–3, equation (11) predicts well the measured pile volume over nearly 4 orders of magnitude, with an r-square value of 0.94 (Figure 11). In comparison to Figure 6, the fit is better in Figure 11 owing to the strong dependence of sediment volume on the dam width cubed, which is encapsulated in the model of (nonnormalized) sediment volume. This comparison does not represent a true prediction as components of equation (11) were fit to data from the same experiments. This notwithstanding, our measurements of pile volume were made independently of the measurements of pile lengths, heights, top angles, and side angles. Thus, differences between equation (11) and the measured pile volumes result from deviations from pyramidal geometry, experimental error, and the robustness of fits used to derive equations (9) and (10). To explore equation (11) and further compare it to measured pile volumes, we evaluate below the relationship between normalized pile volume and slope, friction angle, and sediment size.

[28] From experiment set 1, normalized pile volumes $\frac{V}{(W+D)^3}$ increased with increasing D, but the data show
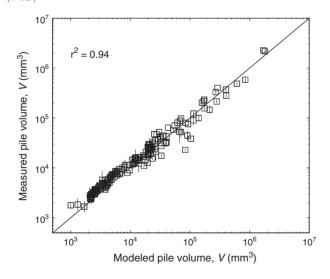

Figure 11. Modeled pile volume from equation (11) versus measured pile volume for all data from experiment sets 1–3. Symbols represent geometric means, and error bars represent one geometric standard deviation from five to eight repeat experiments. In most cases, error bars are smaller than the symbol size. The solid line represents a 1:1 correlation.

significant scatter (Figure 12a). The volumetric data collapse to a single relationship when plotted against $D/(W+D)$, where normalized pile volume was approximately constant for $D/(W+D) < 0.02$ and increased by more than an order of magnitude for large normalized sediment sizes (Figure 12b). This trend exists regardless of whether D was varied (and W was constant) or whether W was varied (and D and all other particle specific properties were constant), showing again that these changes in $\frac{V}{(W+D)^3}$ were fundamentally due to changes in $D/(W+D)$ (Figure 12c). Equation (11) reproduces well the overall trend in the data as well as the apparent scatter about the trend, the latter of which results from small differences in S_r and S_f between the different experiments (Figure 12d). In particular, in the limit of $D/(W+D) \ll 1$ and $W \gg D$, the pile volume is independent of sediment size.

[29] Results from experiment sets 2 and 3 show that normalized pile volumes were greatest at slopes that just exceeded the friction slope (i.e., $\frac{S-S_f}{S_f} \sim 0$), decreased with increasing slope, and approached a constant value for $S \gg S_f$ (Figures 13a and 13b). The data nearly collapse to a single relationship when $\frac{V}{(W+D)^3}$ is plotted against $\frac{S-S_f}{S_f}$ (Figures 13c and 13d). Equation (11) reproduces these trends well. In particular, in the limit of $S \to S_f$, the pile top angle ($\tan\alpha$) approaches S, and therefore, pile volume approaches infinity. This represents the limit of a continuous soil mantle where our model no longer applies. Furthermore, where S is large, the increase in both the pile top and side angles tend to offset each other so that pile volume is nearly independent of slope (Figure 13).

4.6. Extension to Multiple Dams

[30] The results discussed above are applicable to the case of a single sediment dam. On natural hillslopes, multiple neighboring dams (e.g., neighboring stems, neighboring low-lying branches, or neighboring bedrock roughness elements) may interact. To investigate this issue, experiment set 4 was designed to test the effect of two dams of equal width placed next to each other in the slope normal direction. Unless otherwise stated, all references to W in this section refer to the width of a single dam. All the experiments were performed using the Plexiglas table at $S = 0.78$, and $D/(W+D) = 0.091$. Different experiments had different values of λ, the slope-perpendicular distance between the two dams. The experiments were repeated for three different sediment sizes (and therefore three different dam widths, thus holding $D/(W+D)$ constant) to evaluate whether λ alone controls pile interactions, or whether λ/D is the relevant parameter as might be expected if grains bridge the gap [*Cates et al.*, 1998].

[31] Experimental results show that when the gap between the dams was zero ($\lambda = 0$), the normalized pile volume followed the predictions from the single dam experiments if W in equation (11) is set to twice the width of an individual dam (i.e., $V \propto (2W+D)^3$) (Figure 14a). Likewise, as expected, when λ was large, the total volume of trapped particles behind both dams was equal to twice the value expected for a single dam (i.e., $V \propto 2(W+D)^3$) (Figure 14a). Given just these proportionalities, one might expect the volume in the first case to be a factor of 4 larger than the
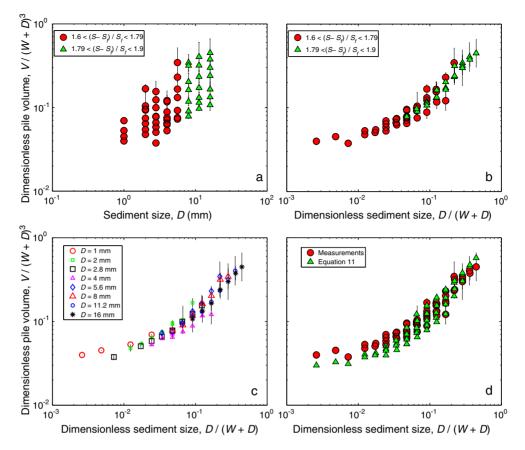
Figure 12. Normalized sediment pile volume versus (a) sediment size and (b–d) normalized sediment size for the case of fixed board slope ($S = 0.78$) and nearly constant normalized slope ($1.64 < (S − S_f)/S_f < 1.9$). The data appear to collapse despite differences in the friction slope in Figure 12b and large differences in sediment diameter in Figure 12c. Figure 12d shows measurements compared to model results following equation (11). Symbols represent geometric means, and error bars represent one geometric standard deviation from five to eight repeat experiments. Symbols without error bars either are from a single experiment or have an error less than the symbol size.

volume in the second case. The data show, however, that the total trapped sediment volume is only about ~2.4 times larger with $\lambda = 0$ (i.e., a single pile) as compared to the case with a large gap spacing and two separate piles, because the latter had larger pile side angles than the former owing to larger $D/(W + D)$), consistent with the model [equation (11)].

[32] For all cases, the total volume of stored sediment was largest for some intermediate gap spacing, the value of which scaled with sediment diameter (Figure 14a). Normalizing the gap distance by particle diameter results in a collapse of the data with the greatest amount of sediment trapped at $\lambda/D \approx 2$ (Figure 14b). This occurred because for $\lambda/D < 2$, the sediment bridge across the gap was strong enough to support a single pile with dimensions equivalent to what would have formed for the case of a single rigid dam of width $2W + D + \lambda$. Given that sediment volume scales as the cube of dam width, two dams with a small gap in between result in a larger volume of trapped sediment than with $\lambda = 0$. For $2 < \lambda/D < 5$, sediment also bridged the gap, but the bridge was not sufficiently strong to support a pile volume equivalent to a rigid dam with a width $2W + D + \lambda$; instead, the trapped sediment took the form of two overlapping piles. For $\lambda/D > 5$, no sediment bridging occurred, and sediment behind the neighboring dams did

not interact. For cases with mixed sediment sizes, which were not investigated, we expect that the coarser fraction may set the limit for grain bridging.

5. Application to Hillslope Sediment Storage and Postfire Sediment Yield

[33] Our results suggest that significant volumes of sediment can be trapped on slopes that exceed the angle of repose by local roughness such as vegetation. This may explain why, in steep mountain terrain, bare bedrock slopes are relatively rare and instead often maintain a patchy soil mantle [*DiBiase et al.*, 2012]. The first-order control on sediment volume is the basal width of the roughness element; for example, in cases where $W \gg D$, trapped sediment volume scales with the cube of dam width. In addition to this greater-than-linear dependence, W may vary by several orders of magnitude across different landscapes or different plant species [e.g., *Keeley*, 1992], and therefore, it is likely the dominant variable in nature. Sediment size, grain-scale bedrock roughness, and hillslope angle are important secondary effects on sediment trapping, especially where $D/(W + D) > 0.05$ and $\frac{S − S_f}{S_f} < 1$. At the catchment scale,
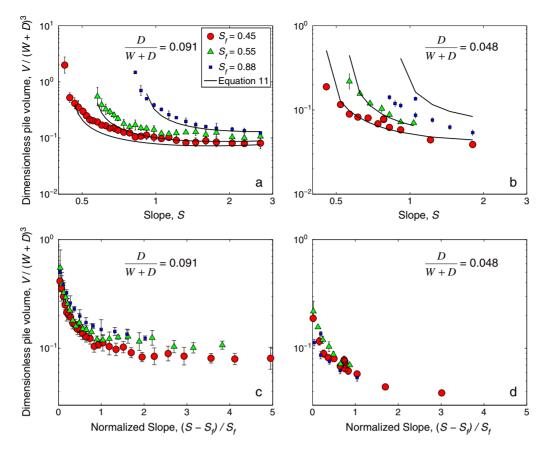
Figure 13. Normalized pile volume for three different board roughness scales (Plexiglas, 0.192 mm sandpaper, and 2.8 mm grain board that correspond to the three friction slopes) as a function of (a) table slope with $D/(W+D) = 0.091$ (experiment set 2), (b) table slope with $D/(W+D) = 0.048$ (experiment set 3), (c) normalized table slope with $D/(W+D) = 0.091$, and (d) normalized table slope with $D/(W+D) = 0.048$. Solid lines in Figures 13a and 13b are model results from equation (11). Symbols represent geometric means, and error bars represent one geometric standard deviation from five to eight repeat experiments. Symbols without error bars either are from a single experiment or have an error less than the symbol size.

however, large vegetation dams, perhaps composed of multiple plants, are likely to dominate sediment storage, and thus, $D/(W+D) < 0.05$ may often be the case [*DiBiase and Lamb*, 2013].

[34] Figure 15 shows contours of $\frac{V}{(W+D)^3}$ following equation (11) for the case of $S_r = S_f = 0.58$ (corresponding to 30°), which may represent typical values in natural landscapes. For slopes common to many bedrock landscapes of 35° to 45° [e.g., *Jackson and Roering*, 2009; *DiBiase et al.*, 2010], $D/(W+D)$ can be neglected as a variable if $D/(W+D) < 0.05$ (Figure 15). For this case, equation (11) reduces to

$$V \approx a_5 W^3 \qquad (12)$$

where a_5 varies by about a factor of 2, from 0.04 to 0.02, for slopes between 35° and 45° (Figure 15). There are several factors we have not investigated that could be important in determining the trapping capacity of vegetation in nature, including root growth and binding, cohesion, rainfall, and mixed particle sizes. The only field data on vegetation trapping capacity we are aware of show good agreement with equation (12) with $a_5 \approx 0.06$ for a variety of plant types and basal plant widths ($0.2 < W < 2$ m) on unburned slopes in the semiarid San Gabriel Mountains, CA [*DiBiase and*

Lamb, 2013], suggesting that our experiments may be capturing the dominant effects in some field cases. While equation (12) may be an appropriate approximation of equation (11) for many landscapes, it is important to recognize that a_5 may increase by more than an order of magnitude as slope approaches the friction slope (i.e., for slope angles that approach 30° in Figure 15). Thus, the friction slope is a key parameter that needs to be assessed in different landscapes when applying equation (11), as it can deviate from 30° due to variability in particle shape (e.g., angularity) and roughness of the underlying substrate.

[35] Experimental results suggest that terrain that exceeds the friction angle may be the largest contributor to postfire dry ravel, consistent with field observations [*Bennett*, 1982; *Gabet*, 2003; *Roering and Gerber*, 2005; *Jackson and Roering*, 2009; *Lamb et al.*, 2011]. Moreover, our results offer an explanation for the nearly immediate dry ravel response following wildfire in steep terrain in the absence of rainfall [*Bennett*, 1982; *Rice*, 1982] and observations of newly exposed bedrock following wildfire [*Jackson and Roering*, 2009; *Schmidt et al.*, 2011; *DiBiase and Lamb*, 2013]. In steep bedrock landscapes, sediment is inherently unstable, and stability can be provided locally by vegetation. Upon incineration, trapped sediment can be transported rapidly downslope
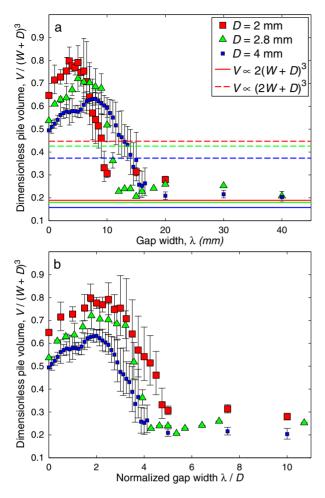
Figure 14. Dimensionless pile volume as a function of (a) gap width and (b) normalized gap width for the case of two side-by-side dams from experiment set 4. Pile volumes are normalized by the width of a single dam. All experiments had a constant table slope ($S = 0.78$), a smooth Plexiglas table with a nearly constant board friction slope ($1.64 < (S - S_f)/S_f < 1.75$), and a constant value of normalized particle diameter ($D/(W+D) = 0.091$). In Figure 14a, the dashed lines show model predictions from equation (11) for the case of zero gap spacing (i.e., with a dam width of $2W + D$), and the solid lines show model predictions from equation (11) for the case of two dams of width $W + D$ with noninteracting sediment piles. Different colors correspond to different sediment diameters. Symbols represent means, and error bars represent one standard deviation from five to eight repeat experiments. Symbols without error bars either are from a single experiment or have an error less than the symbol size.

coming to rest only on lower sloping soil-mantled hillslopes or in channels. The rapid loading of mountain channels with relatively fine-grained material (e.g., sand and fine gravel) may explain the heightened sediment yield following wildfire and the propensity for debris flows following rainfall due to in-channel sediment-bed failure and bulking [e.g., *Kean et al.*, 2011]. Thus, predictions of wildfire-induced sediment yield and debris flows in steep bedrock landscapes may be improved by focusing measurements and modeling on transient sediment storage prior to wildfire and, in particular, on basal plant width (including stems, low-lying branches, and litter) within
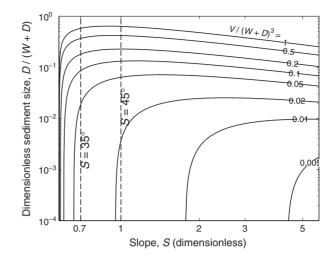

Figure 15. Contours of normalized pile volume as a function of dimensionless sediment diameter and slope as given by equation (11) for the case of $S_f = S_r = 0.58$ (corresponding to 30°). Also shown are slopes of 35° and 45° that bound that range of hillslope angles typical of bedrock landscapes.

parts of the landscape with hillslopes that exceed the angle of sediment stability and are connected to the channel network. As explored by *Lamb et al.* [2011], the rate of sediment production from bedrock, the rate of vegetation regrowth, and the time since last burn may also affect postfire sediment yield if vegetation dams are not filled to capacity with sediment at the time of wildfire. In addition, there may be incomplete release of sediment depending on the burn severity [e.g., *DiBiase and Lamb*, 2013].

[36] The maximum sediment yield from wildfire-induced release of trapped sediment on steep bedrock slopes can be estimated from mass balance by the product of vegetation density (c_0) and the sediment-trapping capacity of individual plants (V) [*Lamb et al.*, 2011]. *DiBiase and Lamb* [2013] used equation (8), $\tan \alpha = \tan \gamma = S_f = 0.58$ (i.e., 30°), and $c_0 = 0.5$ plants/m^2 [*Keeley*, 1992] to estimate the maximum potential fire-induced ravel yield for a ~2 km^2 region of the front range of the San Gabriel Mountains, CA. They considered ravel storage only for slopes ranging from 30° to 45° (where the local slope was measured using 1 m resolution laser altimetry data), based on field observations that local slopes less than 30° have a continuous soil mantle, and hillslopes steeper than 45° have sparse vegetation and are rocky [*DiBiase et al.*, 2012]. They calculated that the maximum amount of transiently stored sediment on these steep bedrock hillslopes is equivalent to about 35 mm of soil (or 14 mm of rock, using measured average bulk soil density of 1100 kg/m^3 and inferred organic content of 40%) spread evenly over the landscape or approximately 28 years of soil production (using a soil production rate of ~0.5 mm/yr) [*Heimsath*, 1999; *Heimsath et al.*, 2012; *DiBiase and Lamb*, 2013]. Using our new scaling relationship based on the laboratory experiments [equation (11)], we repeated this analysis on the same catchment as *DiBiase and Lamb* [2013] using $D/(W+D) \ll 1$ (e.g., $D/(W+D)$ is typically $< 10^{-4}$ based on field measurements), $S_r = 0.76$ (which is the average of 10 repeat measurements ($\sigma = 0.6°$) of field sediment using the dam-break method [*Vanburkalow*,

1945]), and $S_f = 0.58$ (based on field observation of continuous soil mantle for slopes less than 30°). Compared to equation (8) with $\tan \alpha = \tan \gamma = S_f = 0.58$ as in *DiBiase and Lamb* [2013], equation (11) predicts slightly lower sediment storage on slopes just greater than the friction slope, and the result is that the calculated maximum amount of transiently stored sediment for this area of the San Gabriel Mountains is equivalent to about 20 mm of soil (8 mm of rock) spread evenly over the hillslope or about 16 years of soil production. These calculations illustrate the high potential for a significant amount of transiently stored sediment by vegetation dams on bedrock slopes.

[37] Predicting catchment-scale sediment yield requires incorporating other processes besides local vegetation dams such as sediment transport on soil-mantled hillslopes and in channels. Nonetheless, our scaling analysis implies, in comparison to background soil production rates, an order of magnitude increase in sediment yield following wildfire, which is consistent with the observed ~10-fold increase in catchment-scale sediment yield in the 1–2 years following wildfire as measured from debris basins along the San Gabriel Mountain front range [*Lave and Burbank*, 2004; *Lamb et al.*, 2011]. This suggests that vegetation dams in this landscape may often be near capacity, that vegetation regrowth is fast and fire frequency is low relative to the time scales of dam refilling [*Lamb et al.*, 2011], and that transport of fire-induced pulses of sediment through channels is relatively rapid. Therefore, the grain-scale and plant-scale mass balance modeling proposed herein may inform directly larger catchment-scale predictions of postfire sediment yield.

[38] Over geomorphic time scales, it remains an open question as to whether wildfire influences landscape evolution in steep bedrock landscapes, or whether it simply modulates the transient storage and release of sediment on hillslopes. In other words, will increased fire occurrence lead to enhanced denudation rates over geomorphic time scales? In soil-mantled landscapes, hillslope sediment flux, soil thickness, and soil production from bedrock are intimately linked [*Heimsath et al.*, 1997; *Anderson*, 2002] so that changes in soil flux induced by fire can affect landscape evolution [*Roering and Gerber*, 2005]. It is unclear if the same feedbacks exist on bedrock slopes with patchy soil cover and where transport processes (e.g., vegetation storage and release of sediment) are highly nonlocal [*Gabet and Mendoza*, 2012]. The fact that bedrock slopes exist that exceed the threshold for stability of loose sediment draws into question the applicability of local transport-limited soil-flux models that predict infinite flux at such slopes [*Roering et al.*, 1999; *Gabet*, 2003]. In these supply-limited landscapes, soil production from bedrock may be controlled by processes unrelated to soil depth [*Heimsath et al.*, 2012], which may in turn decouple sediment flux from landscape evolution.

6. Conclusions

[39] Controls on sediment flux in steep bedrock landscapes may be significantly different than in soil-mantled landscapes due to slopes that exceed the friction angle for sediment stability, as well as local sediment trapping by vegetation dams. In this study, we developed a theoretical framework and performed a series of tilt-table experiments to build a semiempirical model for the maximum sediment storage upslope of local roughness, such as vegetation, on steep hillslopes that otherwise exceed the angle for sediment stability. The first-order control on trapped sediment volume is the width of the vegetation dam, with volume scaling with the cube of dam width. For cases where the dam width is less than about 50 grain diameters in length, the ratio of particle diameter to dam width is also an important control on pile volume. Large relative particle diameters result in pile side angles that exceed significantly the angle of repose, likely due to enhanced particle-force chains, which ultimately produce larger pile volumes. Pile volumes are greatest for slopes that just exceed the friction slope for sediment stability and decrease with increasing slope, mostly as a result of a reduced top angle of the sediment pile with increasing slope. However, trapped sediment volumes are independent of slope for gradients greater than about twice the friction slope; for these large slopes, both the pile top and side angles depend on slope, but these effects largely cancel out. For the case of multiple neighboring sediment dams, grains bridge gaps with a spacing less than about five grain diameters. This results in a single sediment pile that is significantly larger than the sum of the individual sediment piles that form for cases with larger gap spacing. The maximum amount of sediment is trapped when the gap spacing is about two grain diameters in length. Overall, our results provide a new framework to quantify sediment transport on steep hillslopes as a highly nonlocal process of sediment storage and release. This process may explain the rapid increase in hillslope sediment yield observed following wildfire in steep terrain and in the absence of rainfall as sediment dams are incinerated.

References

Anderson, H. W., G. B. Coleman, and P. J. Zinke (1959), Summer slides and winter scour: Dry-wet erosion in southern California, *Rep. 36*, pp 1–12, U.S. Forest Service, Pacific and Southwest Forest and Range Experimental Station, Berkeley, Calif.

Anderson, R. S. (2002), Modeling the tor-dotted crests, bedrock edges, and parabolic profiles of high alpine surfaces of the wind river range, Wyoming, *Geomorphology*, 46(1–2), 35–58, doi:10.1016/s0169-555x(02)00053-3.

Bennett, K. A. (1982), Effects of slash burning on surface soil erosion rates in the Oregon Coast Range, PhD dissertation, 70 pp., Oregon State Univ., Corvallis.

Buffington, J. M., W. E. Dietrich, and J. W. Kirchner (1992), Friction angle measurements on a naturally formed gravel streambed—Implications for critical boundary shear-stress, *Water Resour. Res.*, 28(2), 411–425, doi:10.1029/91wr02529.

Burbank, D. W., J. Leland, E. Fielding, R. S. Anderson, N. Brozovic, M. R. Reid, and C. Duncan (1996), Bedrock incision, rock uplift and threshold hillslopes in the northwestern Himalayas, *Nature*, 379(6565), 505–510, doi:10.1038/379505a0.

Cannon, S. H., J. E. Gartner, M. G. Rupert, J. A. Michael, A. H. Rea, and C. Parrett (2010), Predicting the probability and volume of postwildfire debris flows in the intermountain western United States, *Geol. Soc. Am. Bull.*, 122(1–2), 127–144, doi:10.1130/b26459.1.

Cates, M. E., J. P. Wittmer, J. P. Bouchaud, and P. Claudin (1998), Jamming, force chains, and fragile matter, *Phys. Rev. Lett.*, 81(9), 1841–1844, doi:10.1103/PhysRevLett.81.1841.

Clarke, B. A., and D. W. Burbank (2010), Bedrock fracturing, threshold hillslopes, and limits to the magnitude of bedrock landslides, *Earth Planet. Sci. Lett.*, *297*(3–4), 577–586, doi:10.1016/j.epsl.2010.07.011.

DiBiase, R. A., K. X. Whipple, A. M. Heimsath, and W. B. Ouimet (2010), Landscape form and millennial erosion rates in the San Gabriel Mountains, CA, *Earth Planet. Sci. Lett.*, *289*(1–2), 134–144, doi:10.1016/j.epsl.2009.10.036.

DiBiase, R. A., A. M. Heimsath, and K. X. Whipple (2012), Hillslope response to tectonic forcing in threshold landscapes, *Earth Surf. Proc. Land.*, *37*(8), 855–865, doi:10.1002/esp.3205.

DiBiase, R. A., and M. P. Lamb (2013), Vegetation and wildfire controls on sediment yield in bedrock landscapes, *Geophys. Res. Lett.*, *40*, 1–5, doi:10.1029/2013GL055108.

Eaton, E. C. (1935), Flood and erosion control problems and their solution, Am. Soc. Civ. Eng. Trans., *101*, 1302–1330.

Estep, J., and J. Dufek (2012), Substrate effects from force chain dynamics in dense granular flows, *J. Geophys. Res.*, *117*, F01028, doi:10.1029/2011jf002125.

Florsheim, J. L., E. A. Keller, and D. W. Best (1991), Fluvial sediment transport in response to moderate storm flows following chaparral wildfire, Ventura County, southern California, *Geol. Soc. Am. Bull.*, *103*(4), 504–511.

Foufoula-Georgiou, E., V. Ganti, and W. E. Dietrich (2010), A nonlocal theory of sediment transport on hillslopes, *J. Geophys. Res.*, *115*, F00A16, doi:10.1029/2009jf001280.

Fu, X. (2004), A physical model of dry ravel movement, dissertation, Washington State Univ., Pullman.

Furbish, D. J., M. W. Schmeeckle, and J. J. Roering (2008), Thermal and force-chain effects in an experimental, sloping granular shear flow, *Earth Surf. Proc. Land.*, *33*(13), 2108–2117, doi:10.1002/esp.1655.

Gabet, E. J. (2003), Sediment transport by dry ravel, *J. Geophys. Res.*, *108*, 2049, doi:10.1029/2001JB001686.

Gabet, E. J., and T. Dunne (2003), A stochastic sediment delivery model for a steep mediterranean landscape, *Water Resour. Res.*, *39*(9), 1237, doi:10.1029/2003wr002341.

Gabet, E. J., and M. K. Mendoza (2012), Particle transport over rough hillslope surfaces by dry ravel: Experiments and simulations with implications for nonlocal sediment flux, *J. Geophys. Res.*, *117*, F01019, doi:10.1029/2011jf002229.

Gartner, J. E., S. H. Cannon, P. M. Santi, and V. G. Dewolfe (2008), Empirical models to predict the volumes of debris flows generated by recently burned basins in the western US, *Geomorphology*, *96*(3–4), 339–354, doi:10.1016/j.geomorph.2007.02.033.

Heimsath, A. M., W. E. Dietrich, K. Nishiizumi, and R. C. Finkel (1997), The soil production function and landscape equilibrium, *Nature*, *388*(6640), 358–361, doi:10.1038/41056.

Heimsath, A. M. (1999), The soil production function, dissertation, 324 pp., Univ. of Calif., Berkeley.

Heimsath, A. M., R. A. DiBiase, and K. X. Whipple (2012), Soil production limits and the transition to bedrock-dominated landscapes, *Nat. Geosci.*, *5*(3), 210–214, doi:10.1038/ngeo1380.

Jackson, M., and J. J. Roering (2009), Post-fire geomorphic response in steep, forested landscapes: Oregon Coast Range, USA, *Quat. Sci. Rev.*, *28*(11–12), 1131–1146, doi:10.1016/j.quascirev.2008.05.003.

Kean, J. W., D. M. Staley, and S. H. Cannon (2011), In situ measurements of post-fire debris flows in southern California: Comparisons of the timing and magnitude of 24 debris-flow events with rainfall and soil moisture conditions, *J. Geophys. Res.*, *116*, F04019, doi:10.1029/2011jf002005.

Keeley, J. E. (1992), Demographic structire of California chaparral in the long-terms absence of fire, *J. Veg. Sci.*, *3*(1), 79–90.

Korup, O. (2006), Rock-slope failure and the river long profile, *Geology*, *34*(1), 45–48, doi:10.1130/g21959.1.

Korup, O., and F. Schlunegger (2007), Bedrock landsliding, river incision, and transience of geomorphic hillslope-channel coupling: Evidence from inner gorges in the Swiss Alps, *J. Geophys. Res.*, *112*(F3), F03027, doi:10.1029/2006jf000710.

Krammes, J. S. (1965), Seasonal debris movement from steep mountainside slopes in southern California, *Federal Interagency Sedimentology Conference*, U.S. Dept. of Agriculture.

Los Angeles County Flood Control District (LACFCD) (1959), Report on debris reduction studies for mountain watersheds of Los Angeles County, 164 pp, Report of the Los Angeles County Flood Control District, Los Angeles, CA.

Lamb, M. P., W. E. Dietrich, and L. S. Sklar (2008), A model for fluvial bedrock incision by impacting suspended and bed load sediment, *J. Geophys. Res.*, *113*(F3), F03025, doi:10.1029/2007jf000915.

Lamb, M. P., J. S. Scheingross, W. H. Amidon, E. Swanson, and A. Limaye (2011), A model for fire-induced sediment yield by dry ravel in steep landscapes, *J. Geophys. Res.*, *116*, F03006, doi:10.1029/2010jf001878.

Lave, J., and D. Burbank (2004), Denudation processes and rates in the transverse ranges, southern California: Erosional response of a transitional landscape to external and anthropogenic forcing, *J. Geophys. Res.*, *109*(F1), F01006, doi:10.1029/2003jf000023.

Moody, J. A., and D. A. Martin (2001), Initial hydrologic and geomorphic response following a wildfire in the Colorado Front Range, *Earth Surf. Proc. Land.*, *26*(10), 1049–1070.

Perron, J. T., J. W. Kirchner, and W. E. Dietrich (2009), Formation of evenly spaced ridges and valleys, *Nature*, *460*(7254), 502–505, doi:10.1038/nature08174.

Rice, R. M. (1982), Sedimentaion in the chaparral: How do you handle unusual events?, in Sediment Budgets and Routing in Forested Drainage Basins, edited by F. J. Swanson, R. J. Janda, T. Dunne and D. N. Swanson, pp. 39–49, U.S. Forest Service Technical Paper, Washington, D. C.

Roering, J. J., J. W. Kirchner, and W. E. Dietrich (1999), Evidence for nonlinear, diffusive sediment transport on hillslopes and implications for landscape morphology, *Water Resour. Res.*, *35*(3), 853–870, doi:10.1029/1998wr900090.

Roering, J. J., J. W. Kirchner, L. S. Sklar, and W. E. Dietrich (2001), Hillslope evolution by nonlinear creep and landsliding: An experimental study, *Geology*, *29*(2), 143–146, doi:10.1130/0091-7613(2001) 029 < 0143:hebnca > 2.0.co;2.

Roering, J. J., and M. Gerber (2005), Fire and the evolution of steep, soil-mantled landscapes, *Geology*, *33*(5), 349–352, doi: 10.1130/g21260.1.

Schmidt, K. M., M. N. Hanshaw, J. F. Howle, J. W. Kean, D. M. Staley, J. D. Stock, and G. W. Bawden (2011), Hydrologic conditions and terrestrial laser scanning of post-fire debris flows in the San Gabriel Mountains, CA, USA, *Ital. J. Eng. Environ.*, 583–593, doi:10.4408/IJEGE.2011-03.B-064.

Shakesby, R. A., and S. H. Doerr (2006), Wildfire as a hydrological and geomorphological agent, *Earth Sci. Rev.*, *74*(3–4), 269–307, doi:10.1016/j.earscirev.2005.10.006.

Sklar, L. S., and W. E. Dietrich (2004), A mechanistic model for river incision into bedrock by saltating bed load, *Water Resour. Res.*, *40*(6), W06301, doi:10.1029/2003wr002496.

Swanson, F. J. (1981), Fire and geomorphic processes, in Fire Regime and Ecosytem Properties, edited by H. A. Mooney, T. A. Bonnicksen, N. L. Christiansen, J. E. Lotan and W. A. Reiners, pp. 401–421, U.S. Forest Service General Technical Report, Washington, D. C.

Tucker, G. E., and G. R. Hancock (2010), Modelling landscape evolution, *Earth Surf. Proc. Land.*, *35*(1), 28–50, doi:10.1002/esp.1952.

Vanburkalow, A. (1945), Angle of repose and angle of sliding friction—An experimental study, *Geol. Soc. Am. Bull.*, *56*(6), 669–707, doi:10.1130/0016-7606(1945)56[669:aoraao]2.0.co;2.

Wells, W. G. (1981), Some effects of brush fires on erosion processes in coastal southern California, in Erosion and Sediment Transport in the Pacific Rim Steeplands, edited by T. R. G. Davies and A. J. Pearce, pp. 305–342, International Association of Hydrological Sciences Christchurch, New Zealand. Pub. 132. Washington, DC:.

Wells, W. G. (1987), The effect of fire on the generation of debris flows in southern California, *Rev. Eng. Geol.*, *7*, 105–114.